Low-frequency incremental permeability for the evaluation of deep carburization treatments: Theoretical understanding

Benjamin Ducharne, Yves Armand Tene Deffo, Gael Sebald, Tetsuya Uchimoto, Christophe Gallais, Olivier Ghibaudo

Low-frequency incremental permeability for the evaluation of deep carburization treatments: Theoretical understanding

Benjamin Ducharne[1], Yves Armand Tene Deffo[2], Gael Sebald[1], Tetsuya Uchimoto[3], Christophe Gallais[4], Olivier Ghibaudo[4].

[1] ELyTMaX IRL3757, CNRS, Univ Lyon, INSA Lyon, Centrale Lyon, Université Claude Bernard Lyon 1, Tohoku University, Sendai, Japan.

[2] Faculty of Engineering and Technology, University of Buea, Buea P.O. Box 63, Cameroon.

[3] Tohoku University, Institute of Fluid Science IFS, Sendai 980-8577, Japan.

[4] Audit et R&T Industriels, SAFRAN TRANSMISSION SYSTEMS, Colombes, France.

Abstract

Precise evaluation of deep carburization treatments is essential to prevent degradation of high-performance mechanical components. A nondestructive magnetic method called low-frequency incremental permeability testing appears to be particularly suitable for this purpose. This method consists of slowly magnetizing the specimen to be controlled and then superimposing a relatively low-frequency eddy current testing process on the specimen (<2 kHz). The sensor's coil impedance is monitored along with the magnetization cycle. When plotted versus the magnetic excitation, the impedance produced butterfly-shaped curves that were dependent on the carburization depth. Operating at low frequency increases the scanned layer thickness up to the untreated inner part of the specimen and induces characteristic variations in the butterfly-shaped curves. A model to solve for the indirect relationship between the magnetic properties and the carburization treatment properties is presented in this manuscript. This model combines the Dodd and Deeds analytical expression for a flat sensor coil above a two-layer conductor with Jiles-Atherton theory for consideration of the hysteresis. The magnetic and electromagnetic responses are well considered, providing accurate reconstructions of experimental data. The model predictions reveal magnetic indicators that are highly correlated with the carburization depth and provide optimal conditions for nondestructive testing observation.

Keywords

Metallurgical surface treatment, magnetic incremental permeability, magnetization mechanisms.

I - Introduction

Metallurgical surface treatments are applied to metallic component surfaces to enhance their resistance to corrosion and/or wear. Widely used techniques include shot peening and carburization [1]. Carburization causes iron or steel part surfaces to harden by absorbing carbon during heating in a carbon-bearing gas such as carbon monoxide. This process helps to prevent corrosion by producing a hard layer called a case with a thickness called the case depth (CD) [2]. The CD can range from 200 µm to 5 mm and the surface hardness can reach 900 HV (Vickers hardness). These hardness levels are required in various applications, including gears, bearings, and camshafts [3]-[5]. The CD is dependent on the processing time and temperature. In general, longer carburizing times and higher temperatures typically increase the carbon diffusion depth and the surface hardness [6].

The CD must be monitored precisely throughout the manufacturing process for quality inspection purposes. However, most industrial CD evaluation tests are destructive. These methods involve sectioning, polishing, and measuring the hardness of the sample at regular depth intervals until it falls below a threshold value (typically around the 550 HV level for conventional steel [7]). This method is efficient, but is both destructive and time-consuming.

Nondestructive methods are also available, such as the ultrasonic guided wave method, which is based on the proportionality between Lamb wave attenuation and the hardness [8]. This technique is accurate, but the blind zone that occurs close to the emitter reduces the method's applicability. Other nondestructive methods include [9]-[11] the isotropic radiation method, thermal techniques, eddy current testing, direct-current potential drop measurement, and X-ray fluorescence. These methods require significant quantities of experimental data to feed the

multi-variant regressions that are used to return the CD evaluation indirectly. However, many of these methods have largely remained in use within an academic framework.

Magnetic methods also exist and their development is at a more advanced stage. Industrial equipment based on these magnetic techniques, including the Stresstech Rollscan® and the IZFP 3MA® (Micromagnetic, Multi-parametric, Microstructure, and stress Analysis) system from the Fraunhofer Institute, have already been commercialized. The Rollscan® device uses magnetic Barkhausen noise (MBN) analysis [12]. When correctly set, this device has proven to be accurate even for thick CD evaluations (>3.5 mm). Nevertheless, the origins of these good correlations are questionable. Recent papers have explored the reading depth of MBN and demonstrated maxima of 200 µm on single-phase semi-hard ribbons [13][14], 100 µm on tempered steel, and 40 µm on mild steel [14]. Therefore, we can legitimately question how strongly these top-surface measurements (<200 µm) can be correlated with thick CD treatments (>1 mm). Many hypothetical reasons for the correlation can be proposed, including the trajectory of the surface stress acting like a mirror in reflecting the deep surface treatments. The numbers and distributions of pinning sites (including precipitates and dislocations) as another reason for the correlation is discussed in [15]. The MBN is definitively not a direct image of the CD and many influential factors (including internal stress, grain size, texture, plastic strain, phase changes, and impurities) can potentially modify it. Although promising correlations have been observed, the generalizability of these correlations have still to be confirmed.

The IZFP 3MA® provides a pragmatic and efficient alternative to the Stresstech Rollscan® [16]-[18]. During its learning phase, the 3MA® system collects data from different experimental magnetic observations (including MBN, magnetic incremental permeability (MIP), and harmonic

analysis (HA) measurements). Then, the system establishes a correlation formulation (in the form of a mathematical expression) between the magnetic indicators and the CD that has been pre-characterized via hardness tests. The 3MA® system can achieve unprecedented correlation rates when the experimental conditions are well controlled. Otherwise, the correlation can fall dramatically. Once again, the generalizability of this method is limited [19].

Among the various magnetic responses measured using the 3MA® system, the MIP is worthy of further investigation. The MIP exhibits exciting properties, including a configurable scanning depth that is potentially large enough to allow thick carburization treatments to be observed directly. According to the literature [20]-[22], the MIP is defined as the slope of the inner asymmetric magnetic hysteresis loops (see Fig. 1, left-hand side). These loops, which are also called minor cycles, are obtained when the material under test is exposed to superimposition of two magnetic contributions:

- A quasi-static contribution (DC contribution), i.e., a very low-frequency (f_{DC} < 10 mHz) high-amplitude magnetic excitation (H > 5Hc, where Hc is the coercivity) that provides a bias magnetization.
- A high-frequency contribution (AC contribution, f_{AC} > 1000f_{DC}), i.e., a low-amplitude magnetic excitation that allows measurement of the MIP denoted by μ_{MIP}. The relative expression for μ_{MIPr} is given in Eq. (1):

$$\mu_{\mathrm{MIP_r}} = \frac{1}{\mu_0} \cdot \frac{\Delta \mathrm{B}}{\Delta \mathrm{H}} \tag{1}$$

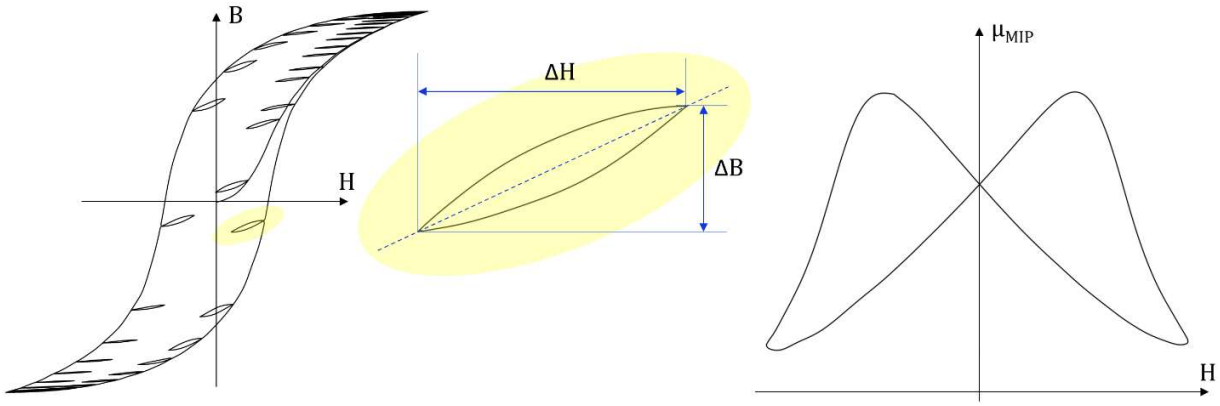

Fig. 1 – MIP illustration and equation.

Here, *B* is the magnetic flux density averaged through the tested specimen's cross-section (as illustrated in the experimental setup of Fig. 2 and described in detail in section II – Experimental conditions). In the nondestructive testing (NDT) context, a magnetic yoke brings *H* up to the surface to be controlled. A magnetic sensor (i.e., a Hall probe or a giant magnetoresistance sensor [23][24]) is used to measure this field locally. Ideally, the DC and AC contributions should be superimposed to act in the same direction using wrapped coils. However, these coils are impossible to set for the inspection of larger components, and in the 1980s, the IZFP Fraunhofer Institute introduced an NDT approach into practice [25] that was based on eddy current testing (ECT) and use of an eddy current pick-up coil. In this alternative method, the flat ECT coil is positioned perpendicular to the surface to be tested (see the illustration in Fig. 3). An ECT controller monitors the coil impedance throughout the magnetization cycle.

The relationship between the MIP and the flat coil signal is indirect. The only way to solve it undergoes space discretization of the Maxwell equation together with a hysteretic material law or analytical expression such as the Dodd and Deeds one later described in this paper. In practice, μ_{MIP} is always replaced with the sensor coil impedance modulus $|Z|$ [26]. The accuracy of this

approach when compared with the exact theoretical model based on the definition has not been investigated thoroughly in scientific research nor validated via academic studies. However, this method has been adopted by most of the NDT community, with focus falling on the magnetization mechanisms involved [27]-[33], and the results were good enough for the MIP-based method to be industrialized in the 3MA® controller [34].

The MIP scan depth is linked to the AC contribution frequency and can be approximated using the skin depth equation:

$$\delta = \sqrt{\frac{2}{\omega\mu\sigma}} \tag{2}$$

where $\mu = \mu_0 \times \mu_r$ is the permeability, $\omega = 2\pi f$ is the angular frequency, and σ is the electrical conductivity. Solution of Eq. (2) in the low-frequency range (f = 1 kHz) and for typical ferromagnetic steel properties ($\sigma = 1\times10^7$ S·m^{-1}, $\mu_{MIPr} = 50$) gives a depth of 1 mm. The skin depth is large enough to overpass even thicker carburization depth treatments.

Low-frequency MIP tests on specimens treated using carburization present very unusual behavior, including a butterfly curve with double inflection points [35]. Detailed analysis of these curves allows for definition of specific indicators that show high correlations to the carburization level. For example, in our previous work [36], multiple magnetic methods were tested (including the $B(H)$ hysteresis cycle and MBN methods) on rod specimens that had been treated with different carburization levels. No significant correlation was observed, other than a sudden change in the slope of the butterfly loops of the treated rod specimens when the excitation field was close to the core coercivity (of similar magnetic behavior to that of untreated specimens) and f = 1 kHz. This local slope showed a remarkable linear correlation coefficient of 0.987 versus the carburization depth.

Although these correlated behaviors are not questionable, they remain qualitative and/or are based on destructive test observations, and further advancements will be necessary to assess and understand these relationships properly. Therefore, in this study, we describe a simulation tool that combines a Dodd and Deeds-based analytical expression for a flat sensor coil located above a two-layer conductor to determine the electromagnetic relationships with the Jiles-Atherton (J-A) model to address the evolution of the magnetic properties. The two conductive layers include a carburized layer and a virgin layer.

Magnetic measurements of the virgin and fully carburized specimens are performed first to set the J-A parameters. Then, the J-A model is run, which provides the Dodd and Deeds simulations with the time-dependent permeabilities required for their resolution.

This study was organized as follows: the model and its parameters were set up first, and comparisons with the MIP responses of carburized specimens were then used for validation. Finally, the model was used to confirm the correlations and provide an adequate assessment of the relationships between the magnetic properties and the carburization thickness.

II – Experimental conditions

2.1) Tested specimens

A series of plate specimens were tested in this work (see the example in Fig. 2). All specimens were made from 16NiCrMo13 martensitic stainless steel [37]. The chemical composition and the physical properties of 16NiCrMo13, which were acquired from the literature, are given in Table 1.

16NiCrMo13 chemical composition (mass fraction wt.%):

Element	Si	S	P	Ni	Mo	Mn	Cu	Cr	C	Al
min	0.15	-	-	3	0.2	0.3	-	0.8	0.13	-
max	0.40	0.02	0.025	3.5	0.3	0.6	0.35	1.1	0.17	0.05

16NiCrMo13 physical properties:

	Poisson's coefficient	*Heat Capacity*	*Thermal conductivity*	*Density*	*Electrical resistivity*	*Expansion coefficient*	*Young modulus*	*Yield $R_{p0.2}$*	*Tensile R_m*	*Elongation*
Unit	-	$J{\cdot}Kg^{-1}{\cdot}°C^{-1}$	$W{\cdot}m^{-1}{\cdot}°C^{-1}$	-	$\mu\Omega{\cdot}cm$	C^{-1}	Gpa	Mpa	MPa	%
Typical value	0.3	484	62	7.87	10	$11.5\ 10^{6}$	200	1000	1300	13

Table 1 –Chemical composition and mechanical and physical properties of 16NiCrMo13 specimens.

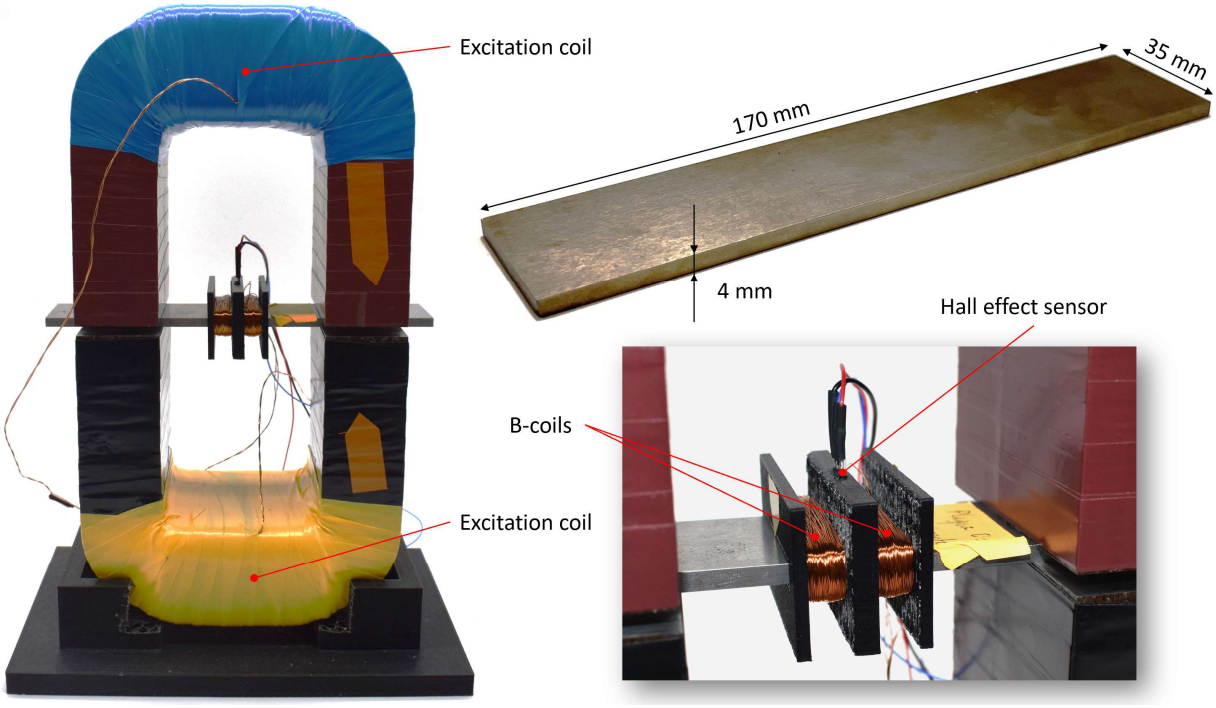

Fig. 2 – Dimensions of the plate-shaped specimens, photograph of the magnetic testing support, and photograph of the magnetic sensors in a *B*(*H*) configuration.

The specimens were divided into four groups. The first group, which was called the “control group,” remained untreated; the other groups were submitted to incrementally increasing carburization processes that led to the surface hardness levels given in Table 2, which were measured from 1 kg load Vickers hardness tests. The hardness threshold defining the CD was set at 580 HV according to Safran Company standards established after multiple destructive tests.

Sample number	CD (mm)	
1	-	**control group**
2	-	
3	0.632	**medium treatment**
4	0.683	
5	0.629	
6	0.643	
7	0.877	**Deep treatment**
8	0.861	
9	1.149	**Very deep treatment**
10	1.105	
11	1.142	

Table 2 – CD estimation results obtained by destructive Vickers hardness characterization.

Because the adjustment of the simulation parameters required experimental data to be acquired from a fully carburized specimen, sample 6 was extracted from the medium treatment group and subjected to additional carburization treatment until it reached a saturated state. The magnetic characterization results for this sample were subsequently used as fully carburized specimen reference values.

2.2) Characterization setup

2.2.1 - Magnetic excitation

The magnetic inductor was made from two U-shaped FeSi 3 wt.% yokes. The leg dimensions of these yokes were 71 mm × 37 mm, and the inner distance between the legs was 70 mm (see

Fig. 2 for an illustration). Two ≈2000-turn excitation coils connected in series were wrapped around the yokes and power was supplied by a Kikusui PCR2006WEA power amplifier (Kikusui Electronics Corp., Japan) driven using a frequency generator (Tektronix AFG1022, USA). The number of turns of each coil was adjusted precisely to avoid dissymmetry in the excitation field distribution. The setup described in this sub-section is used for both B(H) and Z(H) measurements.

2.2.2 - Magnetic instrumentation

a) B(H) major hysteresis cycles

For all magnetic tests, the tangential magnetic field *H* was measured locally on the surfaces of the test specimens in the field direction using a Hall effect sensor (SS94A, Honeywell, Charlotte, NC, USA). This sensor was pre-characterized using a Helmholtz coil driven using a current source in DC mode. Then, a 3D printed support was wrapped with two *n/2* = 200 turn search coils connected in series, as illustrated in Fig. 2. The voltage drop *e(t)* along these search coils caused by the magnetic flux variations was recorded using a Sirius® acquisition card (Dewesoft, Slovenia). The magnetic flux density *B* was then obtained via numerical integration of this electromotive force (using Eq. (3), where *S* is the cross-sectional area). A numerical correction was then perform to cancel the undesired drift caused by the ambient noise and the integration process.

$$\mathrm{B(t)} = -\frac{1}{2n \cdot S}\int_0^{\mathrm{t}} \mathrm{e(t)} \cdot \mathrm{dt} \tag{3}$$

b) $Z_{MIP}(H)$, MIP butterfly cycles

Figure 3 illustrates the pick-up coil used to induce the high-frequency contribution to the MIP measurements. The physical and geometrical properties of this sensor are presented in Table 3:

Inner diameter	$Ø_{in}$ = 5.25 mm
Outer diameter	$Ø_{out}$ = 9.25 mm
Height	h = 9 mm
Lift-off	LO = 1.3 mm
Wire thickness	$Ø_{th}$ = 0.05 mm
Turns number	N = 692
Static resistance	R_{DC} = 18.2 Ω

Table 3 –Physical and geometrical properties of the pick-up coil.

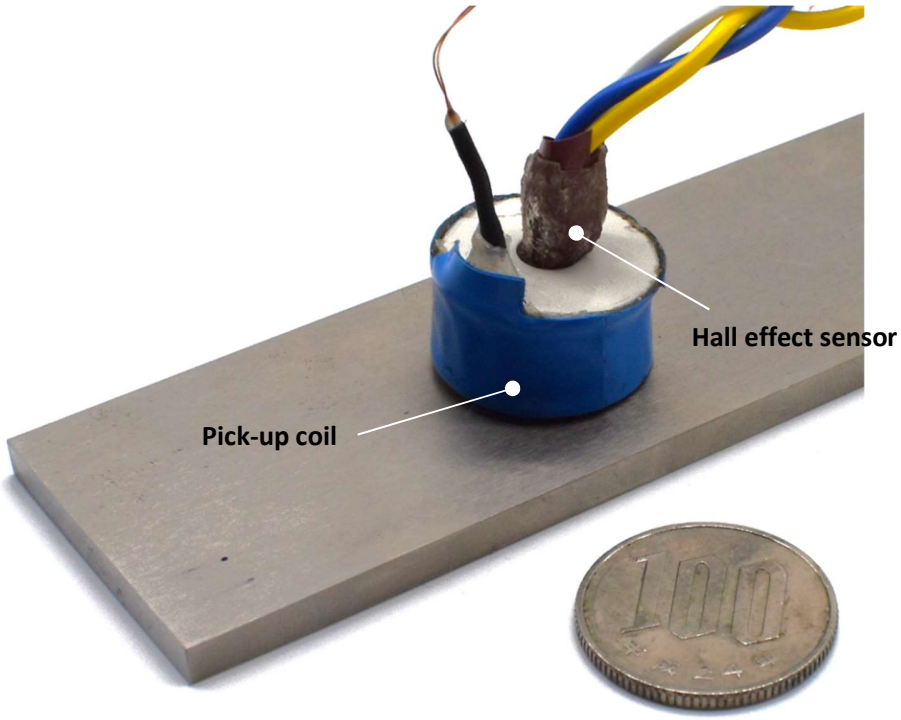

Fig. 3 – Surface sensors used to perform the MIP characterization.

The pick-up coil's impedance was monitored along with the magnetization cycle using an HP4194A LCR-meter (Hewlett Packard, USA), an NI-PCIe-6321 acquisition card, and Labview software (both National Instruments, USA). The LCR-meter's output voltage was set at 0.5 V, thus inducing a magnetic excitation that was lower than one quarter of the coercivity (as recommended in the literature [38]). Within this configuration, the Hall effect probe for the measurement of the surface field *H* was placed at the center of the pancake coil (see Fig. 3). This sensor was the same as the one used for the B(H) curve. The measurement of the B(H) curves were done first followed by the Z(H) ones.

III – Simulation methods

3.1) Jiles-Atherton model for simulation of the magnetic quantities

In the early 1980s, D.C. Jiles and D.L. Atherton published a series of articles entitled "Theory of ferromagnetic hysteresis." These papers provided the theoretical fundamentals of the so-called Jiles-Atherton (J-A) hysteresis model. The model was originally developed to simulate magnetic flux density variations within a ferromagnetic laminate under unidirectional magnetic excitation [39][40] (i.e., in the model, the magnetic excitation *H* and the magnetization state *M* are assumed to be collinear). The J-A model has faced many justified criticisms with regard to its thermodynamic inconsistency and the related accommodation issue (i.e., the model is incapable of simulating closed minor loops [41]). However, the richness of this theory lies in the combination of its limited numerical time resolution and limited number of parameters.

The main equations of the J-A model are recalled below:

_ the magnetization *M* is decomposed into a reversible M_{rev} and an irreversible M_{irr} contribution [39].

$$\mathrm{M} = \mathrm{M}_{\mathrm{rev}} + \mathrm{M}_{\mathrm{irr}} \tag{4}$$

_ H_e is the effective field. H_e includes the external magnetic excitation *H* and an additional contribution related to *M* modulated by α, which is a mean-field parameter:

$$\mathrm{H}_{\mathrm{e}} = \mathrm{H} + \alpha \cdot \mathrm{M} \tag{5}$$

_ The anhysteretic magnetization (M_{anh}) is defined using an analytical expression, such as a Langevin-type equation (Equation 6) or a sigmoid-type function (Equation 7):

$$\mathrm{M}_{\mathrm{anh}} = \mathrm{M}_{\mathrm{s}} \cdot \left[\coth\left(\frac{\mathrm{H}_{\mathrm{e}}}{\mathrm{a}}\right) - \frac{\mathrm{a}}{\mathrm{H}_{\mathrm{e}}}\right] + \mathrm{b} \cdot \mathrm{H}_{\mathrm{e}} \tag{6}$$

$$\mathrm{M}_{\mathrm{anh}} = \mathrm{M}_{\mathrm{s}} \cdot \tanh\left(\frac{\mathrm{H}_{\mathrm{e}}}{\mathrm{a}}\right) \tag{7}$$

M_s is the magnetization saturation and a is the anhysteretic magnetization trajectory parameter.

_ The anhysteretic, irreversible, and reversible magnetizations are linked using Eq. (8), where *c* is a proportionality coefficient:

$$\mathrm{M}_{\mathrm{rev}} = \mathrm{c} \cdot (\mathrm{M}_{\mathrm{anh}} - \mathrm{M}_{\mathrm{irr}}) \tag{8}$$

_ Equation (9) links the anhysteretic magnetization, the irreversible magnetization, and *k*, which is a proportional parameter:

$$\frac{\mathrm{dM}_{\mathrm{rev}}}{\mathrm{dH}_{\mathrm{e}}} = \frac{\mathrm{c} \cdot (\mathrm{M}_{\mathrm{anh}} - \mathrm{M}_{\mathrm{irr}})}{\mathrm{k}\zeta} \tag{9}$$

where ζ is a directional parameter that ensures consistency in the energetic balance:

$$\begin{cases} \zeta = 1 & \text{if } \frac{\mathrm{dH}}{\mathrm{dt}} \geq 0 \\ \zeta = -1 & \text{if } \frac{\mathrm{dH}}{\mathrm{dt}} < 0 \end{cases} \tag{10}$$

_ Combining Eqs. (4) to (9) leads to an analytical expression for d*M*/d*H* (Eq. (11)), which can be assimilated into the differential permeability (μ_{diff}) if we suppose that d*M*/d*H* >> 1:

$$\frac{\mathrm{dM}}{\mathrm{dH}} = \frac{(1-c)\cdot\frac{\mathrm{dM_{irr}}}{\mathrm{dH_e}} + c\cdot\frac{\mathrm{dM_{anh}}}{\mathrm{dH_e}})}{1-\alpha\cdot(1-c)\cdot\frac{\mathrm{dM_{irr}}}{\mathrm{dH_e}} - \alpha\cdot c\cdot\frac{\mathrm{dM_{anh}}}{\mathrm{dH_e}})} \approx \mu_{\mathrm{diff}} \tag{11}$$

_ An integration with respect to *H* gives the average flux density:

$$\mathrm{B} = \mu_0 \cdot \left(\mathrm{H} + \int \frac{\mathrm{dM}}{\mathrm{dH}}.\mathrm{dH}\right) \tag{12}$$

The MIP (as defined in Eq. (1)) can be evaluated quasi-simultaneously by replacing Eq. (5) with System (13) [42]:

$$\begin{cases} \text{if} \quad \mathrm{sign}\left(\frac{\mathrm{dH(t)}}{\mathrm{dt}}\right) = \mathrm{sign}\left(\frac{\mathrm{dH(t-dt)}}{\mathrm{dt}}\right) \\ \mathrm{H_{e_{MIP}}(t)} = \mathrm{H(t-dt)} - \frac{\mathrm{dH(t)}}{\mathrm{dt}} + \alpha \cdot \mathrm{M(t-dt)} \\ \text{else} \\ \mathrm{H_{e_{MIP}}(t)} = \mathrm{H_e(t)} \end{cases} \tag{13}$$

Here, $H_{e\mathrm{MIP}}$ can be regarded as a virtual "effective field" that simulates a change of sign in the magnetic field time derivation. Replacing H_e with $H_{e\mathrm{MIP}}$ in the simulation process leads to a new permeability expression (given as Eq. (9)) that, under the same assumption (i.e., d*M*/dH_{MIP} >> 1), can be assimilated into the MIP (μ_{MIP}; see Eq. (14)):

$$\frac{\mathrm{dM}}{\mathrm{dH_{MIP}}} = \frac{(1-c)\cdot\frac{\mathrm{dM_{irr}}}{\mathrm{dH_{e_{MIP}}}} + c\cdot\frac{\mathrm{dM_{anh}}}{\mathrm{dH_{e_{MIP}}}})}{1-\alpha\cdot(1-c)\cdot\frac{\mathrm{dM_{irr}}}{\mathrm{dH_{e_{MIP}}}} - \alpha\cdot c\cdot\frac{\mathrm{dM_{anh}}}{\mathrm{dH_{e_{MIP}}}})} \approx \mu_{\mathrm{MIP}} \tag{14}$$

Figure 4 illustrates the simulation process by showing a *B*(*H*) hysteresis cycle and the related differential μ_{diff}(H) and MIP μ_{MIP}(H) butterfly loops.

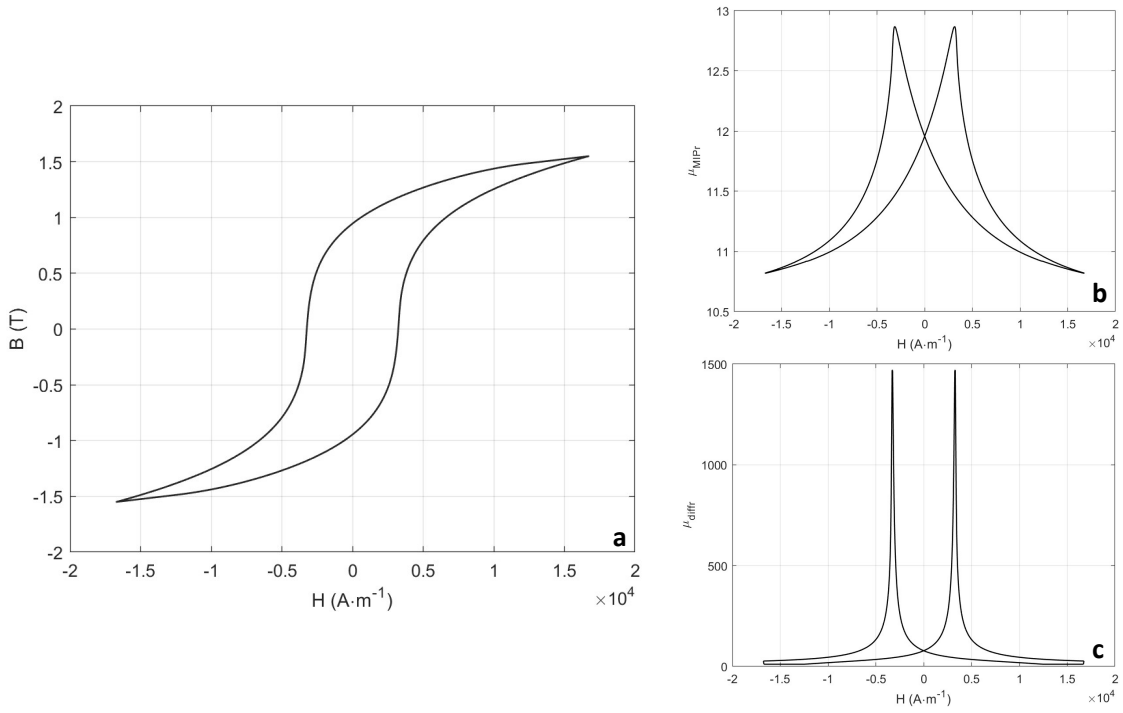

Fig. 4 – a) $B(H)$ J-A model typical hysteresis cycle; b) Differential permeability $\mu_{diffr}(H)$; c) MIP $\mu_{MIPr}(H)$.

Simulation of the MIP and the magnetic quantities in this way is both fast and convenient. The simulation of the minor loops is avoided and the accommodation issue is also resolved. Finally, The experimental process described in section II – Experimental conditions for the measurement of the $IZ_{MIP}(H)I$ butterfly cycles induces magnetic conditions very close to those required by the applicability of the J-A model.

3.2) Dodd and Deeds analytical expression for a coil above a two-layer conductor

The Dodd and Deeds (D&D) analytical expression is a closed-form integral expression for the impedance of a cylindrical coil located above a layered conductive half-space [43]. This expression is used widely in the industrial field to design eddy current tests and optimize parameter measurement processes, including measurements of thickness, conductivity, and

magnetic permeability [44][45]. In our study, we opted to use the D&D analytical solution for a cylindrical coil located above a two-layer conductor. The top layer is the carburized layer, and the bottom layer is the virgin layer. The thickness of the latter layer is considered to be large enough (>3 mm) to be extended to infinity during the simulation process. The D&D solution can be decomposed into two terms. The first term Z_0 is related to the cylindrical coil's imaginary impedance in a vacuum environment:

$$\mathrm{Z_0} = \frac{\mathrm{j2\pi\omega\mu_0}N^2}{(r_2-r_1)^2(z_2-z_1)^2}\int_0^{+\infty}\frac{\chi^2(\mathrm{k}r_1,\mathrm{k}r_2)}{\mathrm{k}^6}\left[\mathrm{k}(z_2-z_1)+\mathrm{e}^{-\mathrm{k}(z_2-z_1)}-1\right]\mathrm{dk} \quad (15)$$

Here, r_1 and r_2 are the coil's inner radius and outer radius, respectively. z_2-z_1 is the coil height (Fig. 5), and N is the number of turns of the coil.

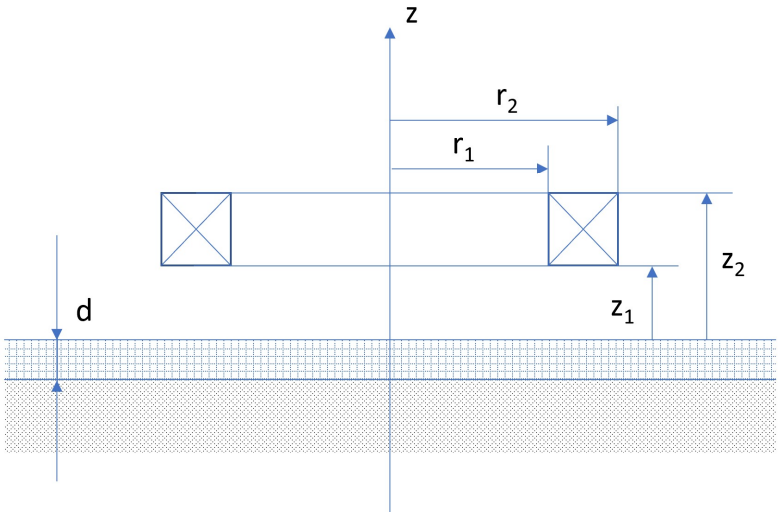

Fig. 5 – Illustration of a cylindrical coil above a two-layer conductive half-space for the D&D simulation.

The second term ΔZ is associated with the impedance changes caused by the two-layer conductor and can be expressed as:

$$\Delta\mathrm{Z} = \frac{\mathrm{j2\pi}\ \ {}_0N^2}{(r_2-r_1)^2(z_2-z_1)^2}\int_0^{+\infty}\frac{\chi^2(\mathrm{k}r_1,\mathrm{k}r_2)}{\mathrm{k}^6}(e^{-kz_1}-e^{-kz_2})^2\frac{(\lambda_1\mu_{\mathrm{r}2}+\lambda_2\mu_{\mathrm{r}1})(\mathrm{k}\mu_{\mathrm{r}1}-\lambda_1)+\mathrm{e}^{-2\lambda_1\mathrm{d}}(\lambda_1\mu_{\mathrm{r}2}-\lambda_2\mu_{\mathrm{r}1})(\mathrm{k}\mu_{\mathrm{r}1}+\lambda_1)}{(\lambda_1\mu_{\mathrm{r}2}+\lambda_2\mu_{\mathrm{r}1})(\mathrm{k}\mu_{\mathrm{r}1}+\lambda_1)+\mathrm{e}^{-2\lambda_1\mathrm{d}}(\lambda_1\mu_{\mathrm{r}2}-\lambda_2\mu_{\mathrm{r}1})(\mathrm{k}\mu_{\mathrm{r}1}-\lambda_1)}\mathrm{dk} \quad (16)$$

$$\lambda_{\mathrm{i}} = \sqrt{\mathrm{k}^2+\mathrm{j}\omega\mu_{\mathrm{r_i}}\mu_0\sigma_{\mathrm{i}}}$$

(where d is the top layer thickness; for additional information about the D&D formalism used here, please refer to [44]).

The final expression given as Eq. (17) here includes the static resistance R_{DC}, which supposedly remains unchanged within the frequency range in this study (f < 20 kHz).

$$\mathrm{Z} = \mathrm{R}_{\mathrm{DC}} + \mathrm{Z}_0 + \Delta\mathrm{Z} \tag{17}$$

3.3) Combination of the J-A and the D&D models

The complete model is illustrated graphically using the scheme in Fig. 6. This scheme combines the J-A model for the magnetic quantities with the D&D resolution for the electromagnetic conversion process. The D&D analytical expression for a cylindrical coil located above a two-layer conductor (Eq. (17)) considers the distinct differences between the physical properties of the top and the bottom conductive layers. In our case, the electrical conductivities were measured precisely during pre-processing using specimens 1 and 6 ($\sigma_1 = 0.7\times10^7$ S·m^{-1} for the top layer and $\sigma_2 = 1\times10^7$ S·m^{-1} for the bottom layer).

The model input is defined in step 1 (Fig. 6). This input corresponds to a magnetic excitation increasing at a constant step size ΔH (which is supposed to be low enough to reach an acceptable resolution). In step 2, two distinct J-A models that were set up using the parameters from specimens 1 and 6 are run. These simultaneous resolutions provide step 3 with the values of μ_{MIP1} and μ_{MIP2}, i.e., the top and bottom layer magnetic permeabilities for the D&D model. Step 4 involves plotting the modulus of Z vs. H.

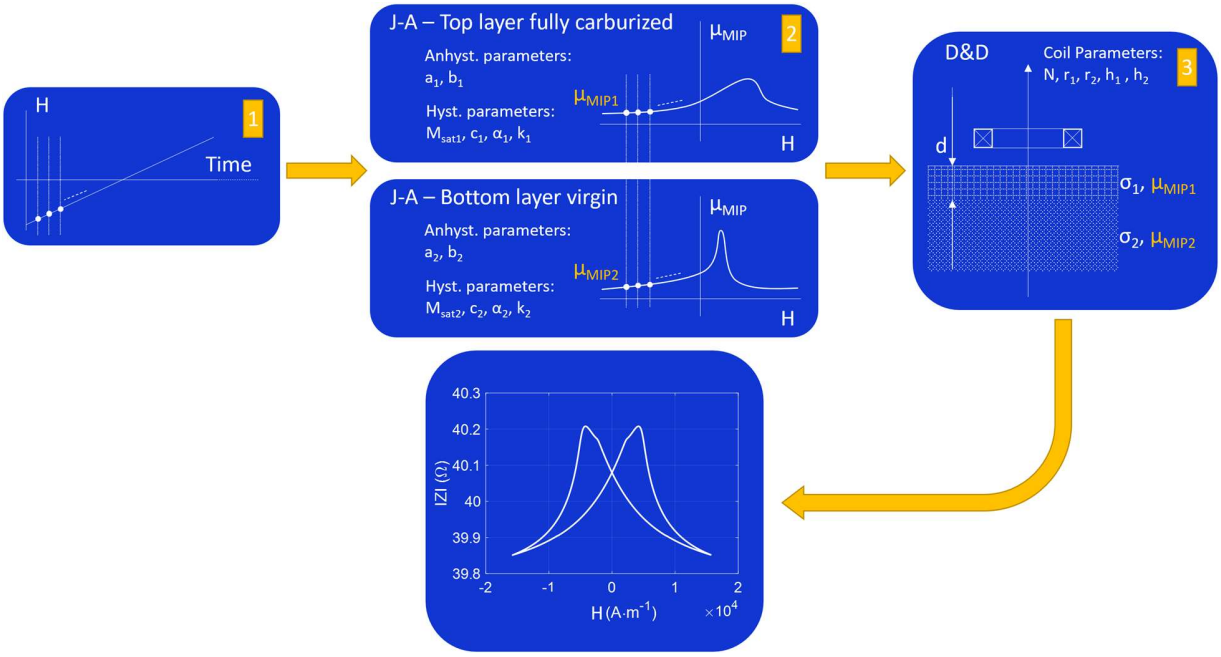

Fig. 6 – Illustration of the D&D simulation process for a cylindrical coil above a layered conductive half-space.

Note that a faster implementation can be obtained by replacing the J-A model with an analytical expression for the $\mu_{MIP}(H)$ curves. However, the physical meaning would be lost, including the possibility of implementing the model using $B(H)$ cycles.

3.4) First experimental characterization and adjustment of simulation parameters

To perform step 2 in Fig. 6 efficiently, precise evaluation of the J-A parameters for specimens 1 and 6 is required. For this evaluation, a first experimental procedure was performed to gather the $B(H)$ and $|Z|(H)$ experimental curves for specimens 1 and 6 (Fig. 7). The excitation frequency of the pancake coil f_{AC} was set at 1 kHz based on the observations in [36], and the hysteresis loop was measured within the low-frequency range (f_{DC} = 100 mHz) because the J-A model does not

consider the frequency effect. An optimization process based on minimization of the relative discrete Euclidean difference (Eq. (17)) error function was then run:

$$\mathrm{RED}_{\mathrm{discrete}}\ (\%) = 100 \cdot \sqrt{\frac{\sum_{i=1}^{m} \left|x_i^{sim} - x_i^{meas}\right|^2}{\sum_{i=1}^{m} \left|x_i^{sim}\right|^2}} \tag{17}$$

Data from the $B(H)$ and $|Z|(H)$ curves were used equally, but more points were considered near the coercivity at which the curves show significant variations. A wide range of values was tested for every J-A parameter and the combination that led to the lowest error was then conserved. Figure 7 depicts comparisons of the simulated and measured results for both specimens, and Table 4 lists the best combinations of the parameters.

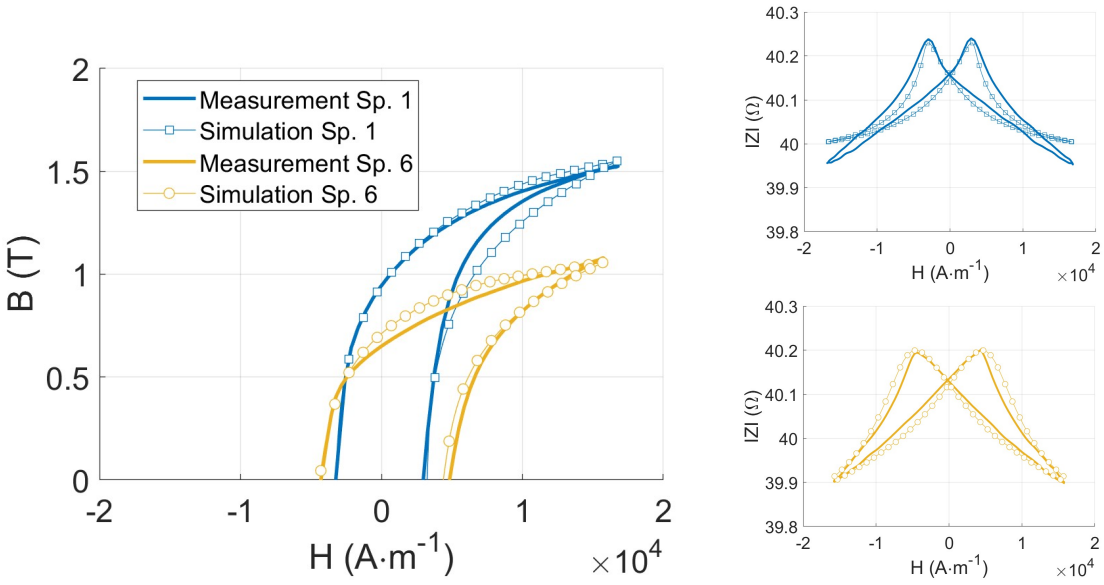

Fig. 7 – Comparison of results of simulations and measurements for the $B(H)$ and $|Z|(H)$ curves for specimens 1 and 6.

J-A Parameters Top layer (Sp. 6)	Typical value	J-A Parameters Bottom layer (Sp. 1)	Typical value
a (A·m^{-1})	11000	a (A·m^{-1})	8300
b	6.8	b	10
Ms (A·m^{-1})	900000	Ms (A·m^{-1})	1110000
k (A·m^{-1})	6500	k (A·m^{-1})	3500
c	0.074	c	0.04
α	0.023	α	0.017

Table 4 –Top (specimen 6) and bottom (specimen 1) layer parameters for the J-A model.

IV – Numerical method usage and practical validation

4.1) Model validation

After the model was configured using the parameters from Table 4, a second experimental procedure was run to check the proposed method's accuracy. The IZI(H) butterfly-shaped curve for one sample of each group in Table 2 was measured at f = 1 kHz and compared with the corresponding simulation results. Figure 8 illustrates these comparisons. At this stage of the process, the top layer thickness d constituted a degree of freedom of the simulation process that could be adjusted to enable better comparisons.

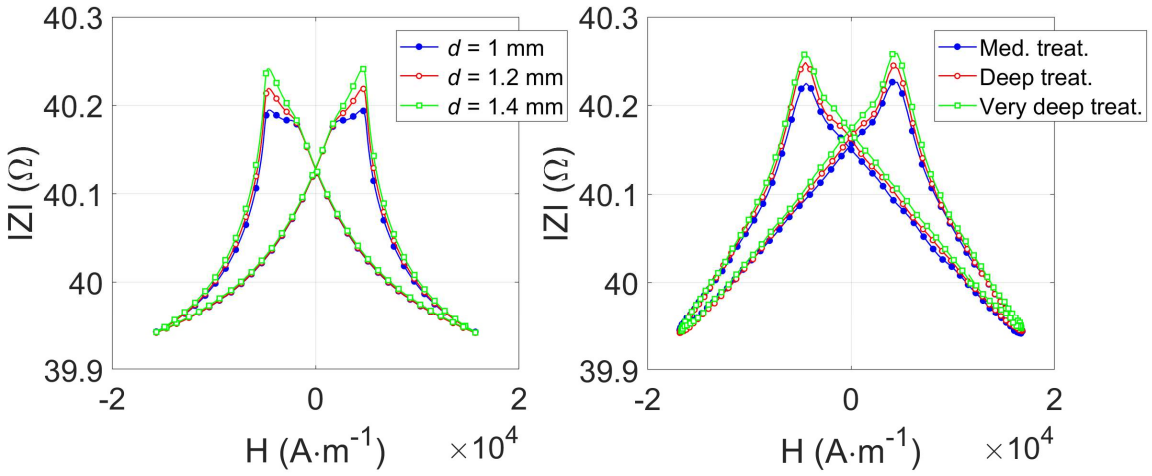

Fig. 8 – a Simulation of the |*Z*|(*H*) curves for d = 1, 1.2 and 1.4 mm. Fig. 8 – b Measurement of the |*Z*|(*H*) curves for the medium, deep, and very deep treatment groups.

In Fig. 8, it is notable that there is a discrepancy between the simulated values of *d* (1, 1.2, and 1.4 mm) and the experimental CD associated with each specimen category (0.65, 0.87, and 1.13 mm, respectively). One possible explanation for these differences lies in the hardness threshold, which was set arbitrarily at 580 HV and was probably overestimated. Other than the medium depth treatment (particularly in terms of the shapes of the peaks), the good general trends observed in Fig. 8 were sufficient to validate the entire simulation process. These results encouraged us to move on to the next stage and use the model's predictive capability.

4.2) Model prediction

Six magnetic indicators were defined (see Fig. 9) and were plotted as a function of *d* (the top layer thickness), which is considered to be the equivalent to the CD in the simulation process.

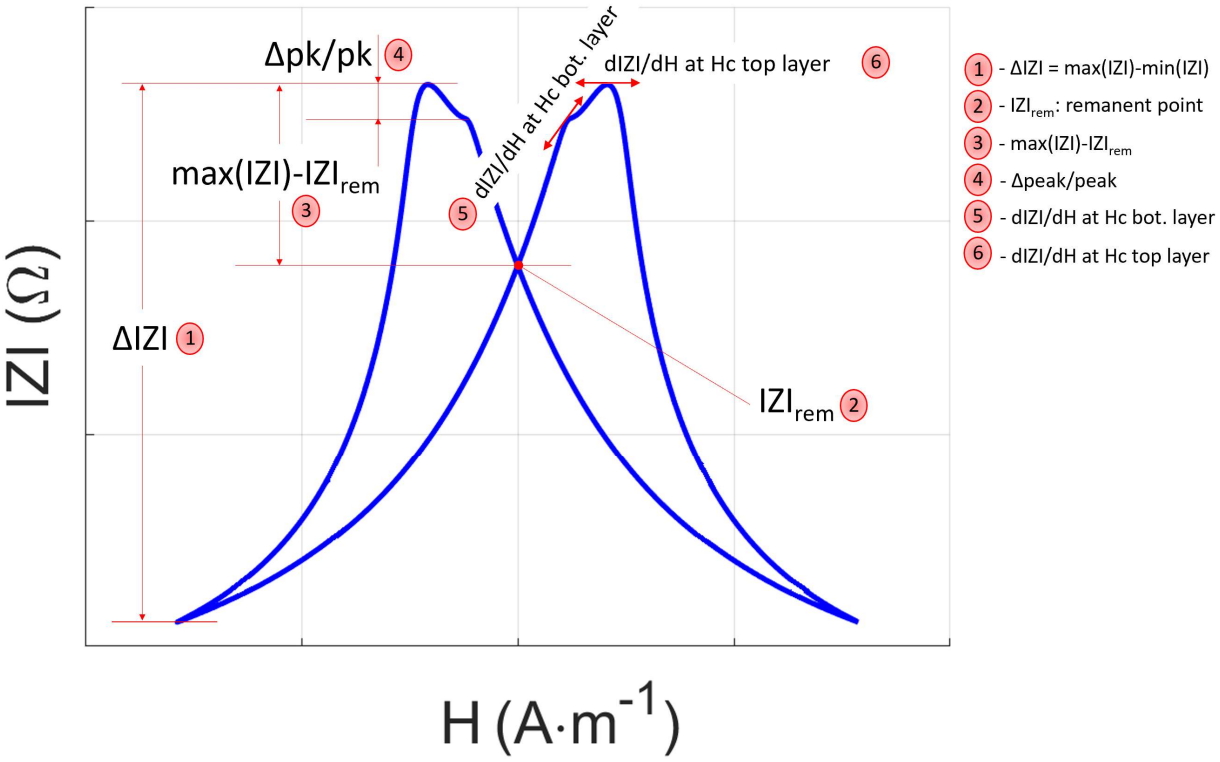

Fig. 9 – List and illustration of the magnetic indicators that were studied for their *d* dependency.

Figure 10 illustrates the model predictions for all tested indicators vs. *d* at *f* = 1 kHz, and Table 5 lists the related Pearson correlation coefficients for *f* ∈ [0.5, 1, 2, 5, 10, and 20] kHz. A minimum local can be seen in the evolution of Δ|Z|(*d*) and (max(|Z|)- |Z_r|)(*d*) for *d* close to 1 10^{-3} m. The origin of this minimum local can be found in the balance between the inner and the upper layer contributions.

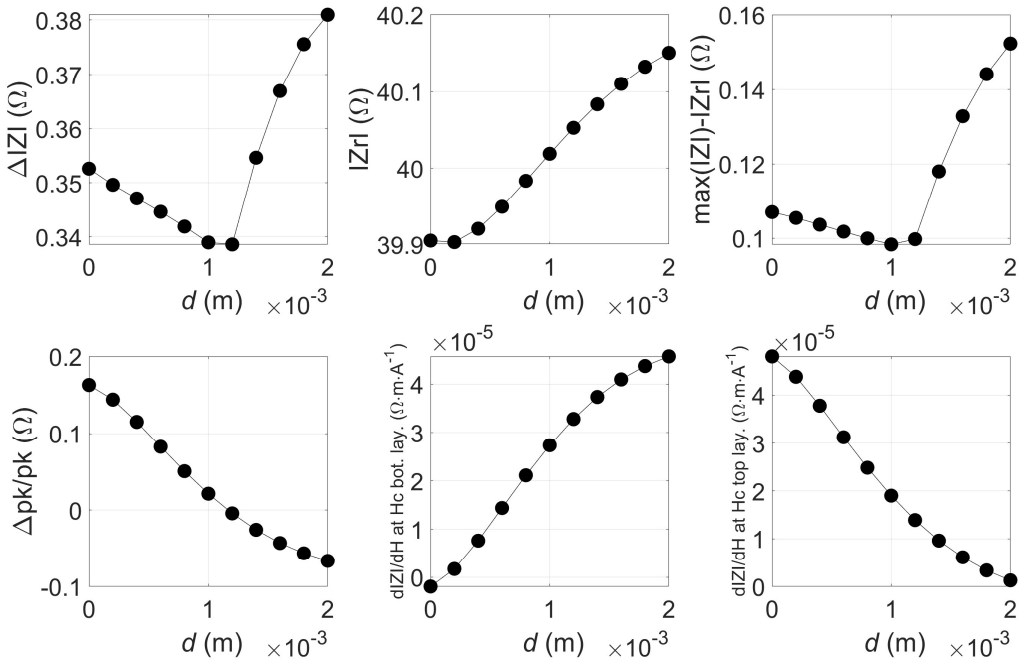

Fig. 10 – Model predictions for all tested indicators vs. *d* at *f* = 1 kHz.

freq (kHz)	0.5	1	2	5	10	20
Magnetic indicators						
ΔIZI = max(IZI)-min(IZI)	0.544	0.665	0.838	0.58	0.479	0.452
IZI_{rem}: remanent point	0.043	0.978	0.958	0.8	0.66	0.556
max(IZI)-IZI_{rem}	0.86	0.779	0.925	0.769	0.617	0.523
Δpeak/peak	0.974	0.99	0.932	0.765	0.637	0.543
dIZI/dH at Hc bot. layer	0.972	0.99	0.928	0.755	0.629	0.538
dIZI/dH at Hc top layer	0.979	0.99	0.935	0.773	0.642	0.546

r : Pearson correlation coefficient

- **r** > 0.95
- 0.95 ≥ **r** > 0.9
- 0.9 ≥ **r** > 0.8
- 0.8 ≥ **r** > 0.7
- **r** ≤ 0.7

Table 5 – Pearson correlation coefficients: magnetic indicators vs. *d*.

The analysis in Table 5 confirms that *f* = 1 kHz is the ideal frequency for use in CD assessment of 16NiCrMo13 martensitic stainless steel. The frequency is small enough to induce a sufficient penetration depth up to the inner core, but is not too small to ensure that the influence of the top layer remains significant. As observed for the rod specimens studied in [36], the slope of the IZI(*H*) curve close to the core coercivity (bottom layer) shows excellent correlation, but this is not

the only parameter. The peak-to-peak distance and the slope at the top layer coercivity are similarly correlated. More unpredictably, with r = 0.978 at f = 1 kHz, the remanence $|Z|_{rem}$ also appears to be an excellent indicator.

4.3) Experimental confirmation of the model predictions

A final experimental procedure was run to confirm the simulation predictions. The $|Z|(H)$ curves for all specimens were measured at f = 1 kHz (Fig. 11). The correlations of the Table 5 indicators with the Table 2 CD pre-characterization parameters were calculated, and the results are depicted in Fig. 12 and listed in Table 6.

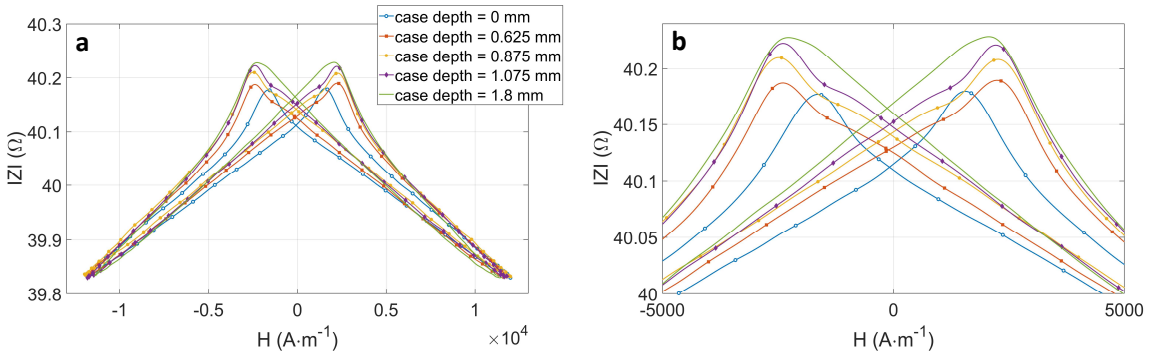

Fig. 11 – a) $|Z|(H)$ experimental measurement for CD ∈ [0 – 1.8] mm; b) same curves zoomed in the coercivity zone.

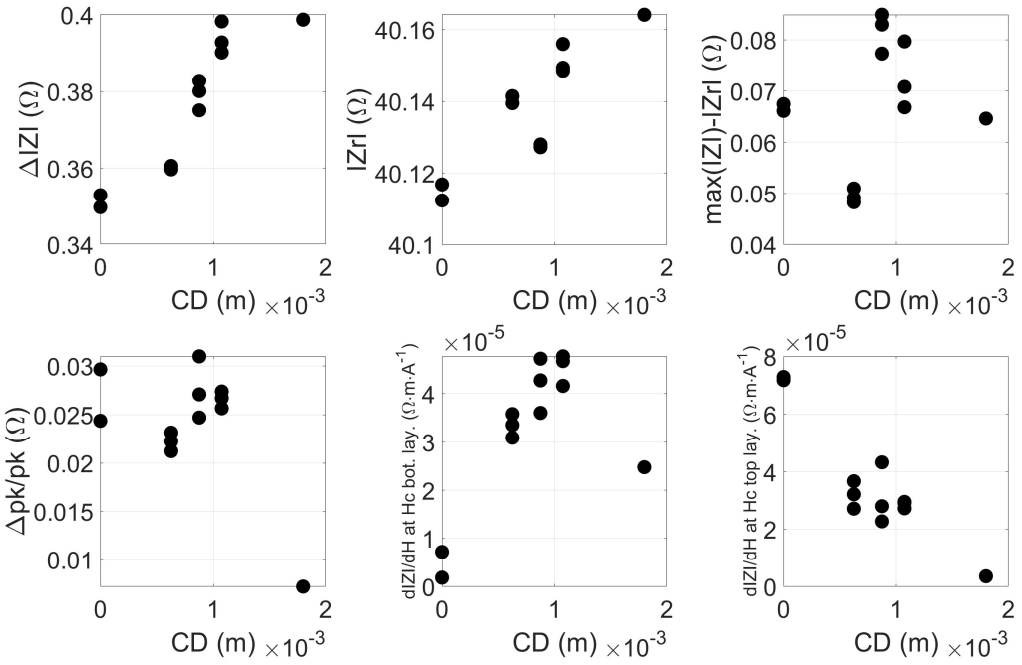

Fig. 12 – Experimental magnetic indicators vs. the CD at f = 1 kHz.

freq (kHz)	1	1
Magnetic indicators		
ΔIZI = max(IZI)-min(IZI)	0.894	0.903
IZI_{rem}: remanent point	0.842	0.772
max(IZI)-IZI_{rem}	0.219	0.348
Δpeak/peak	0.54	0.08
dIZI/dH at Hc bot. layer	0.61	0.964
dIZI/dH at Hc top layer	0.91	0.882

r : Pearson correlation coefficient

- **r** > 0.95
- 0.95 ≥ **r** > 0.9
- 0.9 ≥ **r** > 0.8
- 0.8 ≥ **r** > 0.7
- **r** ≤ 0.7

Without Sp. 6

Table 6 – Pearson correlation coefficients: magnetic indicators vs. CD.

Upon examination, Table 6 confirms some of the expected good correlations, particularly for the slope close to the top layer coercivity and the remanence, even if it is not as high as predicted. However, with r = 0.61 (Table 6, first column), the poor correlation of dIZI/dH at H = Hc bottom

layer is more surprising. The strong influence of specimen 6 in this poor correlation is still worthy of note. A much better value of r = 0.964 (Table 6, second column) was obtained when specimen 6 was removed from the statistical list. Figure 13 shows a better view of this unexpected change in the I*Z*I(*H*) slope vs. CD tendency.

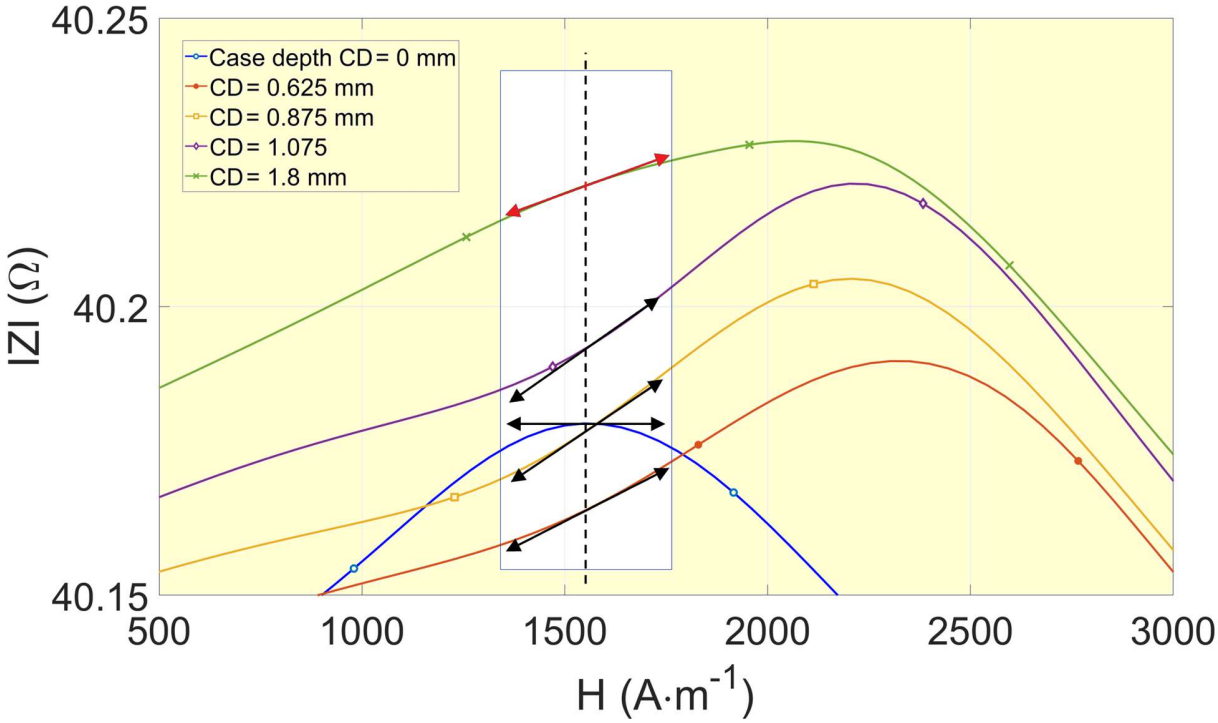

Fig. 13 – Illustration of the d|*Z*|/d*H* slope at $H = H_c$ for the bottom layer vs. CD.

There are various possible causes that could be used to explain this unexpected behavior, including an experimental issue. However, the experimental conditions were the same throughout, and the reproducibility of the magnetic response of specimen 6 was confirmed through additional testing. At *f* = 1 kHz and for CD = 1.8 mm, the influence of the untreated core material on the magnetic properties is weak. The green curve in Fig. 12 reflects the upper layer's magnetic behavior alone, which is harder magnetically speaking (because of the presence of the

carbon and/or internal stress generation). The curve has I*Z*I(*H*) peaks that are less narrow than those of the virgin specimen, thus reducing the overall correlation factor.

If the maximum carburization depth (indicated by the CD) in real-life applications never exceeds 1.2 mm, removal of specimen 6 from the statistical analysis may not have any significant consequences for the industrial application. Because specimen 6 exhibits behavior that deviates from the general trends observed for the other specimens, it is then reasonable to exclude it from the analysis, particularly if its characteristics do not represent the typical CD values encountered in practical applications.

IV – Conclusions

The carburization process is applied to high-performance mechanical components to make their upper layers harder, increase their wear resistance, and help to prevent corrosion. The carburization process and the resulting case depth (CD) must be monitored precisely during the manufacturing process for quality certification. Our previous study [36] showed that low-frequency MIP is a magnetic NDT method that is well suited to this purpose. This magnetic NDT method mainly solicits the domain wall bulging magnetization mechanism (irreversible magnetization), which is the most CD-sensitive mechanism.

At f = 1 kHz, the low frequency allows controlled depth penetration, which enables complete scanning of the carburized layer and provides the ability to reach untreated zones.

In this study, we have tested a series of plate-shaped specimens that were treated using different carburization levels. Each specimen CD was pre-characterized through destructive evaluation of its hardness. Then, a model was designed to predict the low-frequency MIP

response that combined the D&D analytical expression for a flat sensor coil located above a two-layer conductor with the J-A theory for consideration of the hysteresis.

In this model, the thickness of the upper layer *d* was considered to be equivalent to the CD, and the model was used to predict the indirect relationship between the magnetic observations and the destructive pre-characterization of the carburization.

After setting the magnetic parameters for the top and bottom layers, extensive simulations were run, and the results were used as a database to establish correlations between the magnetic indicators and *d*, and thus define the ideal experimental conditions. f = 1 kHz appears to be the most indicative alternative contribution frequency. The slopes at $H = H_c$ of the top and bottom layers were also listed among the highly correlated indicators that confirmed the previous results described in [36].

Then, practical tests were run on all specimens at f = 1 kHz to verify the predictions of the simulations. Most of the good indicators (d|*Z*|/d*H* at the top layer coercivity, remanence) were confirmed to be correct, apart from d|*Z*|/d*H* at the bottom layer coercivity, which showed an unexpected change in the trend for the highly carburized specimen; this was probably due to an additional effect such as the influence of internal stress.

Overall, this study confirmed that the low-frequency MIP technique is a powerful magnetic method for thick CD evaluation. By combining the experimental results with the simulation tool, precise and nondestructive assessments of the CD levels of 16NiCrMo13 specimens treated with unknown carburization treatments were conducted. Furthermore, the simplicity and environmental friendliness of the MIP method make it highly suitable for practical implementation.

Multiple perspectives can be envisaged for the future directions of this work, including:

- From an NDT method viewpoint:

_ All results should be confirmed using specimens with different natures.

_ In addition to carburization, other metallurgical treatments can generate thick layer modifications (e.g., shot peening). Testing our proposed method and the selected indicators on the different configurations from these treatments would also be interesting.

_ In this study, selection of the best indicators was limited to an analysis of the Pearson coefficients that gave linear correlations. However, the nature of the correlation could be nonlinear and could thus lead to different conclusions. Therefore, alternative correlations must be tested in future work.

- From a simulation method viewpoint:

_ A parametric study of the effects of the J-A parameters on the correlations between the magnetic indicators and *d* could provide essential information, including confirmation of the robustness of the proposed method.

_ The D&D analytical expression includes no spatial/local information. However, its resolution can be extended to provide a multilayer consideration in which each layer could be defined with its own permeability and conductivity. Gradients of the magnetic properties that are closer to the actual behavior could be simulated via this discretization.

_ Replacement of the D&D analytical expression with a finite element model represents another exciting possibility, but the local resolution will, unfortunately, mean that longer simulation times will be required.

References

[1] Torres, M.A.S. and Voorwald, H.J.C., 2002. An evaluation of shot peening, residual stress and stress relaxation on the fatigue life of AISI 4340 steel. *International Journal of Fatigue*, *24*(8), pp.877-886.

[2] Genel, K. and Demirkol, M., 1999. Effect of case depth on fatigue performance of AISI 8620 carburized steel. *International Journal of Fatigue*, *21*(2), pp.207-212.

[3] Parrish, G., 1999. *Carburizing: microstructures and properties*. Asm International.

[4] Edenhofer, B., Joritz, D., Rink, M. and Voges, K., 2015. Carburizing of steels. In *Thermochemical Surface Engineering of Steels* (pp. 485-553). Woodhead Publishing.

[5] Rahmel, A., Grabke, H.J. and Steinkusch, W., 1998. Carburization–introductory survey. *Materials and corrosion*, *49*(4), pp.221-225.

[6] Boyle, E., Northwood, D.O., Bowers, R., Sun, X. and Bauerle, P., 2009. Microstructural effects on residual stress, retained austenite, and case depth of carburized automotive steels. *SAE International Journal of Materials and Manufacturing*, *1*(1), pp.697-708.

[7] Mittemeijer, E.J., 2013. Steel Heat treating Fundamentals and Processes. *ASM Handbook A*, *4*, p.2013.

[8] Belanger, P., 2010. *Feasibility of thickness mapping using ultrasonic guided waves* (Doctoral dissertation, Department of Mechanical Engineering, Imperial College London).

[9] Chan, S.C., Grimberg, R., Hejase, J.A., Zeng, Z., Lekeakatakunju, P., Udpa, L. and Udpa, S.S., 2010. Nonlinear eddy current technique for characterizing case hardening profiles. *IEEE transactions on magnetics*, *46*(6), pp.1821-1824.

[10] Bowler, J.R., Huang, Y., Sun, H., Brown, J. and Bowler, N., 2008. Alternating current potential-drop measurement of the depth of case hardening in steel rods. *Measurement Science and Technology*, *19*(7), p.075204.

[11] Guo, X., Sivagurunathan, K., Garcia, J., Mandelis, A., Giunta, S. and Milletari, S., 2009. Laser photothermal radiometric instrumentation for fast in-line industrial steel hardness inspection and case depth measurements. *Applied optics*, *48*(7), pp.C11-C23.

[12] Santa-Aho, S., Vippola, M., Sorsa, A., Leiviskä, K., Lindgren, M. and Lepistö, T., 2012. Utilization of Barkhausen noise magnetizing sweeps for case-depth detection from hardened steel. *Ndt & E International*, *52*, pp.95-102.

[13] Stupakov, A., Perevertov, A. and Neslušan, M., 2020. Reading depth of the magnetic Barkhausen noise. I. One-phase semi-hard ribbons. *Journal of Magnetism and Magnetic Materials*, *513*, p.167086.

[14] Stupakov, A., Perevertov, A. and Neslušan, M., 2020. Reading depth of the magnetic Barkhausen noise. II. Two-phase surface-treated steels. *Journal of Magnetism and Magnetic Materials*, *513*, p.167239.

[15] Holmberg, J., Hammersberg, P., Lundin, P. and Olavison, J., 2023. Predictive Modeling of Induction-Hardened Depth Based on the Barkhausen Noise Signal. *Micromachines*, *14*(1), p.97.

[16] Dobmann, G., 2007. Physical basics and industrial applications of 3MA–micromagnetic multiparameter microstructure and stress analysis. *Fraunhofer IZFP, Saarbrcken, Germany*, pp.1-17.

[17] Mironenko, I., Szielasko, K., Kiselmann, I., Koop, H., Koop, M., Altpeter, I., Dobmann, G. and Boller, C., 2011. Wideband micromagnetic multi-parameter materials characterization with 3MA. In *Proceedings of the 9th International Conference on Barkhausen Noise and Micromagnetic Testing*.

[18] Jedamski, R. and Epp, J., 2020. Non-destructive micromagnetic determination of hardness and case hardening depth using linear regression analysis and artificial neural networks. *Metals*, *11*(1), p.18.

[19] Dobmann, G., Altpeter, I., Wolter, B. and Kern, R., 2008. Industrial applications of 3MA–micromagnetic multiparameter microstructure and stress analysis. *Electromagn. Nondestr. Eval.(XI)*, *31*, pp.18-25.

[20] Gupta, B., Uchimoto, T., Ducharne, B., Sebald, G., Miyazaki, T. and Takagi, T., 2019. Magnetic incremental permeability non-destructive evaluation of 12 Cr-Mo-WV Steel creep test samples with varied ageing levels and thermal treatments. *NDT & E International*, *104*, pp.42-50.

[21] Wilson, J.W., Karimian, N., Liu, J., Yin, W., Davis, C.L. and Peyton, A.J., 2014. Measurement of the magnetic properties of P9 and T22 steel taken from service in power station. *Journal of Magnetism and Magnetic Materials*, *360*, pp.52-58.

[22] Gabi, Y., Jacob, K., Wolter, B., Conrad, C., Straß, B. and Grimm, J., 2020. Analysis of incremental and differential permeability in NDT via 3D-simulation and experiment. *Journal of Magnetism and Magnetic Materials*, *505*, p.166695.

[23] Khan, M.A., Sun, J., Li, B., Przybysz, A. and Kosel, J., 2021. Magnetic sensors-A review and recent technologies. *Engineering Research Express*, *3*(2), p.022005.

[24] Kouakeuo, S.N., Ducharne, B., Solignac, A., Morel, L., Raulet, M.A., Toutsop, B., Deffo, Y.T. and Tsafack, P., 2021. Non-invasive local magnetic hysteresis characterization of a ferromagnetic laminated core. *Journal of Magnetism and Magnetic Materials*, *527*, p.167783.

[25] Dobmann, G., Kern, R., Altpeter, I. and Theiner, W., 1988. Quantitative hardening-depth-measurements up to 4 mm by means of micro-magnetic microstructure multiparameter analysis (3MA). *Review of Progress in Quantitative Non-destructive Evaluation: Volume 7B*, pp.1471-1475.

[26] Zhang, S., Ducharne, B., Takeda, S., Sebald, G. and Uchimoto, T., 2021. Low-frequency behavior of laminated electric steel sheet: Investigation of ferromagnetic hysteresis loops and incremental permeability. *Journal of Magnetism and Magnetic Materials*, *538*, p.168278.

[27] Li, K., Li, L., Wang, P., Liu, J., Shi, Y., Zhen, Y. and Dong, S., 2020. A fast and non-destructive method to evaluate yield strength of cold-rolled steel via incremental permeability. *Journal of Magnetism and Magnetic Materials*, *498*, p.166087.

[28] Burzic, D., Zamberger, J. and Kozeschnik, E., 2010. Non-destructive evaluation of decarburization of spring steel using electromagnetic measurement. *NDT & E International*, *43*(5), pp.446-450.

[29] Matsumoto, T., Uchimoto, T., Takagi, T. and Vertesy, G., 2016. Evaluation of chill structure in ductile cast iron by incremental permeability method. *International Journal of Applied Electromagnetics and Mechanics*, *52*(3-4), pp.1599-1605.

[30] Meilland, P. and Lombard, P., 2018, June. Improvements of Modeling Incremental Permeability in the 3MA System for on-Line Steel Strip Property Assessment. In *Proceedings of the 12th European Conference on Non Destructive Testing. Paper ECNDT-0218-2018. Goteborg, Sweden*.

[31] Martins, C.O.D. and Reguly, A., 2010. MAGNETIC METHODS: Lift-off influence analysis during the micromagnetic stress evaluation of flexible riser tensile armours. *Insight-Non-Destructive Testing and Condition Monitoring*, *52*(6), pp.316-319.

[32] Grimberg, R., Leitoiu, S., Bradu, B.E., Savin, A. and Andreescu, A., 2000. Magnetic sensor used for the determination of fatigue state in ferromagnetic steels. *Sensors and Actuators A: Physical*, *81*(1-3), pp.371-373.

[33] Gupta, B., Ducharne, B., Uchimoto, T., Sebald, G., Miyazaki, T. and Takagi, T., 2021. Comparison of electromagnetic inspection methods for creep-degraded high chromium ferritic steels. *NDT & E International*, *118*, p.102399.

[34] Wolter, B., Gabi, Y. and Conrad, C., 2019. Non-destructive testing with 3MA—An overview of principles and applications. *Applied Sciences*, *9*(6), p.1068.

[35] Yashan, A. and Dobmann, G., 2002. 150 Electromagnetic Non-destructive Evaluation (VI) F. Kojima et al.(Eds.) IOS Press, 2002. *Electromagnetic Non-destructive Evaluation (VI)*, *6*, p.150.

[36] Ducharne, B., Deffo, Y.A.T., Zhang, S., Sebald, G., Lallart, M., Uchimoto, T., Gallais, C. and Ghibaudo, O., 2023. Carburization depth evaluation from magnetic non-destructive testing. *NDT & E International*, *137*, p.102864.

[37] El Ghazal, H., 1999. *Etude des propriétés microstructurales et mécaniques des aciers 16NiCrMo13 cémenté et 32CrMoV13 nitrure: application à la prévision de leur limite d'endurance en fatigue de roulement* (Doctoral dissertation, in France, Lyon, INSA, France).

[38] Matsumoto, T., Uchimoto, T., Takagi, T., Dobmann, G., Ducharne, B., Oozono, S. and Yuya, H., 2019. Investigation of electromagnetic non-destructive evaluation of residual strain in low carbon steels using the eddy current magnetic signature (EC-MS) method. *Journal of Magnetism and Magnetic Materials*, *479*, pp.212-221.

[39] Jiles, D.C. and Atherton, D.L., 1984. Theory of ferromagnetic hysteresis. *Journal of applied physics*, *55*(6), pp.2115-2120.

[40] Jiles, D.C. and Atherton, D.L., 1986. Theory of ferromagnetic hysteresis. *Journal of magnetism and magnetic materials*, *61*(1-2), pp.48-60.

[41] Zirka, S.E., Moroz, Y.I., Harrison, R.G. and Chwastek, K., 2012. On physical aspects of the Jiles-Atherton hysteresis models. *Journal of Applied Physics*, *112*(4), p.043916.

[42] Zhang, S., Ducharne, B., Uchimoto, T., Kita, A. and Deffo, Y.T., 2020. Simulation tool for the Eddy current magnetic signature (EC-MS) non-destructive method. *Journal of Magnetism and Magnetic Materials*, *513*, p.167221.

[43] Dodd, C.V. and Deeds, W.E., 1968. Analytical solutions to eddy-current probe-coil problems. *Journal of applied physics*, *39*(6), pp.2829-2838.

[44] Theodoulidis, T. and Kriezis, E.E., 2006. Eddy Current Canonical Problems (with Applications to Non-destructive Evaluation) Tech Science Press. *Forsyth, GA, USA*, pp.978-0971788015.

[45] Zhang, S., Ducharne, B., Takeda, S., Sebald, G. and Uchimoto, T., 2021. Identification of the ferromagnetic hysteresis simulation parameters using classic non-destructive testing equipment. *Journal of Magnetism and Magnetic Materials*, *531*, p.167971.